Structure Determination of Inactive-State GPCRs with a Universal Nanobody

Michael J. Robertson[1,2], Feng He[1,2], Justin G. Meyerowitz[1,2,3], Alpay B. Seven[1,2], Ouliana Panova[1,2], Maria-Claudia Peroto[1,2], Tao Che[4,5], Georgios Skiniotis[1,2,6]

[1]Department of Molecular and Cellular Physiology, Stanford University School of Medicine, Stanford, CA, USA

[2]Department of Structural Biology, Stanford University School of Medicine, Stanford, CA, USA

[3]Department of Anesthesiology, Perioperative and Pain Medicine, Stanford University School of Medicine, Stanford, CA 94305, USA.

[4]Department of Anesthesiology, Washington University School of Medicine, St. Louis, Missouri, 63110, USA.

[5]Center for Clinical Pharmacology, University of Health Sciences & Pharmacy at St. Louis and Washington University School of Medicine, St. Louis, Missouri, 63110, USA.

[6]Correspondence: yiorgo@stanford.edu

Summary

Cryogenic electron microscopy (cryo-EM) has widened the field of structure-based drug discovery by allowing for routine determination of membrane protein structures previously intractable. However, despite representing one of the largest classes of therapeutic targets, most inactive-state G protein-coupled receptors (GPCRs) have remained inaccessible for cryo-EM because their small size and membrane-embedded nature

impedes projection alignment for high-resolution map reconstructions. Here we demonstrate that a camelid single-chain antibody (nanobody) recognizing a grafted intracellular loop can be used to obtain cryo-EM structures of different inactive-state GPCRs at resolutions comparable or better than those obtained by X-ray crystallography. Using this approach, we obtained the structure of human neurotensin 1 receptor (NTSR1) bound to antagonist SR48692, of μ-opioid receptor (MOR) bound to the clinical antagonist alvimopan, as well as the structure of the previously uncharacterized somatostatin receptor 2 (SSTR2) in the apo state; each of these structures yields novel insights into ligand binding and specificity. We expect this rapid, straightforward approach to facilitate the broad structural exploration of GPCR inactive states without the need for extensive engineering and crystallization.

Introduction

The impact of cryo-EM on structure-based drug discovery has been immense, leading to the characterization of a wide variety of new and valuable membrane protein drug targets, including ion channels and G protein-coupled receptors (GPCRs)[1]. As a key requirement for high-resolution cryo-EM map reconstructions, the randomly oriented particle projections must first be correctly aligned at intermediate-to-low resolution, a step that often fails for small proteins due to their limited structural features. For relatively small membrane proteins, the problem is compounded by the presence of a detergent micelle or lipid nanodisc used for solubilization, which further dampens the contrast of protein densities. This poses a major bottleneck for cryo-EM structure determination of GCPRs, which account for roughly 35% of FDA-approved drugs, with approximately half of those

47 being agonists that activate the receptor and half antagonists or inverse agonists[2] that
48 engage the inactive-state receptor, thereby blocking endogenous signaling. Active-state
49 GPCR structures can be determined in complex with heterotrimeric G protein[3], a ~90 kDa
50 entity that adds significant mass outside the detergent micelle or lipid disc and provides
51 a source of alignment for the transmembrane receptor. However, there is no such
52 generalizable tool for cryo-EM structure determination of inactive-state GPCRs,
53 especially for family A receptors, the largest GCPR subfamily with hundreds of receptors
54 that are typically ~37-50 kDa and lack sizeable extracellular domains for projection
55 alignment. Thus, the application of cryo-EM is severely limited for inactive-state GPCRs,
56 and their structural elucidation mostly relies on extensive engineering and crystallization
57 trials for X-ray studies. This limitation impacts not only mechanistic investigations of
58 GPCRs, but also structure-based drug discovery for the countless therapeutically relevant
59 receptors.

60 Che *et al.*[4] recently reported a camelid VHH domain antibody, referred to as
61 nanobody 6 (Nb6), that engages the inactive-state intracellular loop 3 (ICL3) of the κ-
62 opioid receptor (KOR), even when this loop is grafted onto a wide range of receptors,
63 including orphan receptors and family B receptors. This tool was initially developed as a
64 bioluminescence resonance energy transfer (BRET)-based sensor of receptor activation
65 state, an approach that also allows for cost-effective and robust screening of Nb6-binding
66 constructs by employing BRET assays. Using the Nb6 approach, we obtained three-
67 dimensional (3D) map reconstructions of human NTSR1 (hNTSR1) in complex with Nb6
68 bound to the inverse agonist SR48692[5] at a resolution of 2.4 Å; the mouse MOR bound
69 to a megabody[6], an enlarged nanobody construct derived from Nb6 (Mb6), in complex

70 with the antagonist alvimopan[7] at a resolution of 2.8 Å; and the unliganded (apo) structure
71 of human SSTR2 bound to Nb6 at 3.1 Å resolution. We thus demonstrate that Nb6 is a
72 general solution for determining high-resolution inactive-state structures by cryo-EM.
73 Besides alleviating the need for extensive construct engineering and successful
74 crystallogenesis, the cryo-EM/Nb6 approach comes with two distinct advantages: first, it
75 does not necessitate the screening and development of receptor-specific nanobodies.
76 Second, the Nb6 BRET-based sensor allows for rapid and efficient screening of
77 constructs and conditions instead of time-consuming and expensive cryo-EM-based
78 screening.
79
80 **Employing Nb6 for cryo-EM structure determination of GPCRs**
81 Any fiducial marker that is used for cryo-EM structure determination of a target
82 macromolecule needs to be rigid in its binding and orientation in respect to the structural
83 target. Furthermore, if the marker is particularly small related to the target, it must be
84 positioned such that it provides a distinct feature from various angles to allow
85 unambiguous alignment of the randomly-oriented cryo-EM projections. A crystal structure
86 of Nb6 bound to KOR revealed an interaction at the base of TM5 and TM6, off-center
87 from the major axis of the receptor[4]. We hypothesized that this type of interaction would
88 be an ideal asymmetric fiduciary for cryo-EM particle projection alignment as it would
89 allow for the determination of the rotational orientation of the receptor around its major
90 axis, particularly during initial low-resolution alignments.
91 To evaluate the degree of rigidity of Nb6 when bound to a GPCR, we first
92 performed all-atom molecular dynamics (MD) simulations using the crystal structure of

93 the KOR-Nb6 complex. Alignment of the MD trajectories on the receptor atoms and
94 calculation of the average root mean squared fluctuation (RMSF) for Nb6 atoms over the
95 final 100 ns of triplicate 500 ns simulations (Fig. 1a) showed that Nb6 is rigidly bound and
96 characterized by little flexibility, with the exception of the distal loops at the base of the
97 nanobody.

98 Encouraged by these computational predictions, we proceeded with employing
99 Nb6 for *de novo* cryo-EM structure determination of three pharmacologically relevant
100 family A GPCRs. The first, NTSR1, is broadly associated with neurological and
101 gastrointestinal processes[8]. Overexpression of NTSR1 in some tumor types promotes
102 cancer progression and metastasis and is thus associated with poor prognosis[9],
103 prompting the study and development of NTSR1 inverse agonists for oncology[10]. We also
104 studied MOR, the target of opioids, which are both the most effective treatment for pain
105 but also the therapeutic class underlying the ongoing opioid epidemic in the United
106 States[11]. While current opioid antagonists can treat acute opioid overdose, there is an
107 urgent need for MOR antagonists with improved pharmacokinetic properties[11,12]. Finally,
108 SSTR2 plays a pivotal role in the neuroendocrine system by opposing the release of many
109 hormones, including growth hormone[13]. SSTR agonists are commonly prescribed for
110 neuroendocrine tumors, while SSTR subtype-selective antagonists are in development
111 for diabetes, but the lack of structural information for any somatostatin receptor family
112 member in either active or inactive state has made the development of next-generation
113 SSTR ligands challenging.

114 As described in Che *et al.*, we engineered constructs to enable binding of Nb6 to
115 mouse MOR and human SSTR2 by identifying minimal swaps of ICL3 along with the

116 cytoplasmic tips of transmembrane helix 5 and 6 (TM5/6) with that of the KOR (Fig. 1c).
117 In the case of the closely related MOR, the two point mutations M264L and K269$^{6.24}$R
118 (Ballesteros-Weinstein notation[14]; Fig. 1c) were sufficient to enable Nb6 binding. SSTR2
119 was able to bind Nb6 with the swap of all 15 residues from S238$^{5.68}$ of TM5 (V256$^{5.68}$ of
120 KOR) to K252$^{6.31}$ of TM6 (R270$^{6.31}$ of KOR) (Fig. 1c). For human NTSR1 (hNTSR1) we
121 utilized the same swap from KOR T247$^{5.59}$ to L277$^{6.38}$ as previously described for rat
122 NTSR1[4] (rNTSR1; Fig. 1c). BRET assays of agonist-induced Nb6 dissociation confirmed
123 construct functionality, with all three receptors showing dissociation of the nanobody in
124 response to agonist binding (Fig. 1d-f). In all experimental replicates, the BRET data for
125 MOR response to DAMGO appears to be biphasic, consistent with prior nanobody-based
126 MOR activation sensors[15], where the two-phase response is attributed to distinct plasma
127 membrane and endosomal signaling.
128 High-resolution cryo-EM structure determination was feasible in all cases. Despite
129 Nb6 being only 12 kDa, Nb6, or the equivalent region of Mb6, is resolved in all three
130 maps, providing a critical stable density outside the detergent micelle surrounding
131 NSTR1, MOR and SSTR2. Notably, the local resolution indications for Nb6 in our
132 GPCR/Nb6 complex cryo-EM maps showed high correlation with the relative root mean
133 square fluctuation (RMSF) values for Nb6 calculated from our MD simulations (Fig. 1b).
134 This observation further demonstrates the strong predictive power of MD simulations in
135 assessing the behavior of fiducial markers for such work.
136
137 **Structure of hNTSR1**

138 Obtaining inactive-state crystal structures has proven challenging for NTSR1. The

139 only available crystal structures were determined in 2021[16]: one with receptor in the apo

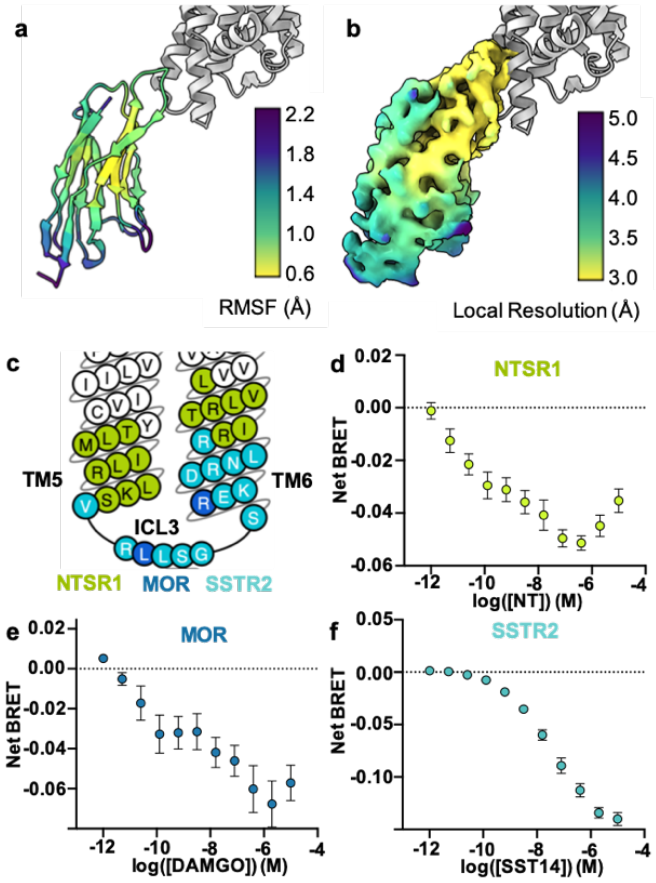

Fig 1. | Construct design and evaluation for Nb6-based GPCR structure determination
a, Root mean squared fluctuations (RMSF) in atomic positions averaged over triplicate molecular dynamics simulations for Nb6 bound to KOR. **b,** Local resolution plot of Nb6 from the cryo-EM map of the SSTR2/Nb6 complex. **c,** Overlay of the three KOR ICL3 constructs used to enable Nb6 binding for MOR (two point mutations), SSTR2 (5.68 to 6.31), and hNTSR1 (5.59 to 6.38). Dose-response data representing loss of BRET (net BRET) between Receptor-rLuc and Nb6-mVenus for **d,** $NTSR1_K$ and neurotensin (NT), **e,** MOR_K and DAMGO, and **f,** $SSTR2_K$ and somatostatin 14 (SST14).

140

141 state (3.19 Å) and two structures with the receptor bound to the inverse agonists SR48692

142 (2.64 Å) or SR142948A (2.92 Å), which are small molecules previously in development

143 for treating cancer. Obtaining these structures required extensive engineering to facilitate

144 protein crystallization, with that work employing a construct of rat NTSR1 evolved in

145 bacteria to acquire numerous thermostabilizing mutations and fused in TM7 with a

146 DARPin[17] protein domain to facilitate crystal packing (rNTSR1-H4)[18]. To assess and

147 compare the cryo-EM/Nb6 approach with crystallography we obtained the cryo-EM

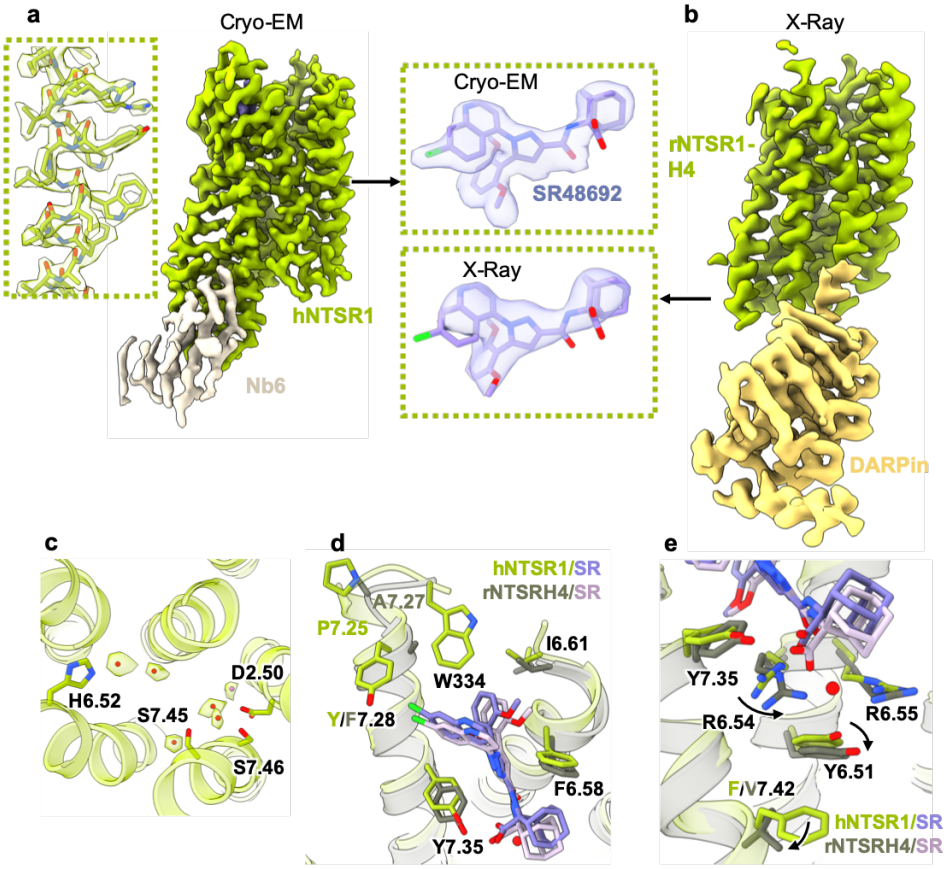

Fig 2. | Comparison of cryo-EM structure of hNTSR1 and crystal structure of rNTSR1-H4

a, Cryo-EM map of hNTSR1 at 2.4 Å global resolution. The arrow points to the cryo-EM density and model for inverse agonist SR48692, the inset to the left is the map-model fit for TM3 **b,** 2Fo-Fc crystallography map of rNTSR-H4 at 2.6 Å contoured at σ=1.0. The arrow points to the Local 2Fo-Fc map around SR48692 contoured at σ=1.25. **c,** Water molecules resolved in the core of the hNTSR1 receptor and their associated cryo-EM densities. **d,** Overlay of the hNTSR cryoEM structure (protein in green, SR48692 in purple) with the rNSTR-H4 crystal structure (protein in gray, SR48692 in pink) highlighting differences in ECL2. **e,** Overlay of the hNTSR cryoEM structure (protein in green, SR48692 in purple) with the rNSTR-H4 crystal structure (protein in gray, SR48692 in pink) highlighting the residue shift and probable loss of bound water molecule caused by the F7.42V thermostabilizing mutation

structure of hNTSR1/Nb6 complex bound to SR48692 (Fig. 2a, Extended Data Fig. 2). Notably, the cryo-EM structure was resolved at a global resolution of 2.4 Å, both a higher nominal resolution than the crystal structure and with significantly better-resolved features, including the density corresponding to the ligand (Fig. 2a, b insets, Extended

152 Data Fig. 8a). This resolution range also reveals densities corresponding to extensive
153 hydration throughout the receptor in the cryo-EM map (Fig. 2c, Extended Data Fig. 3a).
154 The construct for hNTSR1 was minimally modified beyond the KOR ICL3 swap,
155 with only N- and C- termini truncations in regions not resolved in typical family A structures
156 and a single A85$^{1.54}$L mutation to increase expression[19]. While the general ligand pose is
157 very similar between the two structures, the cryo-EM structure reveals additional
158 interactions not observed in the rNTSR-H4 crystal structure. First, the remodeling of the
159 TM7-ECL3 region allows W334 in ECL3 to be resolved in the hNTSR1 structure loosely
160 capping the top of the hydrophobic chloro-naphthyl and dimethoxy-phenyl moieties of
161 SR48692 (Fig. 2c). This change may be due to several amino acid sequence differences
162 at the top of TM7, most prominently P336$^{7.25}$ in hNTSR1 versus T341$^{7.25}$ in rNTSR1-H4,
163 with the proline inducing a sharp turn between the top of TM7 and ECL3 in hNTSR1. In
164 addition, the rearrangement of R327$^{6.54}$ in rNTSR-H4 (R322$^{6.54}$ in hNTSR1) appears to
165 disrupt a water-mediated interaction between R327$^{6.54}$, R328$^{6.55}$ (R323$^{6.55}$ in hNTSR1),
166 and the carboxylate moiety of SR48692 observed in the hNTSR1 structure (Fig. 2d). This
167 R327$^{6.54}$ rearrangement likely stems from the F358$^{7.42}$V thermostabilizing mutation in
168 rNTSR-H4, allowing a downward relaxation of Y324$^{6.51}$ (Y319$^{6.51}$ in hNTSR1) and
169 R327$^{6.54}$. Notable differences also exist in the TM helices between the two structures;
170 TM1 is shifted 3.4 Å further outward from the core of the receptor in the crystal structure
171 (Extended Data Fig. 3b), while the top of TM2 and ECL1 are out of register by one residue.
172 While this may be due to the differences in experimental constructs, the observed
173 discrepancy may also result from the fact that even at σ=1 the 2Fo-Fc map of the crystal
174 structure lacks sidechain information in the ECL1 region, rendering modeling ambiguous

175 (Extended Data Fig. 3c,d). Overall, the lack of thermostabilizing mutations and DARPin
176 in TM7 restores a more native-like inactive state as suggested by the conformation of key
177 amino acids. For example, Y364$^{7.53}$ of the hNTSR1 NPxxY motif (Y369$^{7.53}$ in rNSTR1)
178 occupies a position and rotamer more typical of an inactive state family A GPCR
179 (Extended Data Fig. 3e).
180
181 **Structure of MOR**
182 In parallel, we obtained a cryo-EM structure of the MOR bound to the non-blood
183 brain barrier penetrant, MOR selective inverse agonist alvimopan, an FDA-approved drug
184 for reversing opioid-induced gastrointestinal (GI) symptoms in hospital settings. In the
185 case of NTSR1/Nb6, vitrifying the sample in a very thin buffer layer on holey gold grids[20]
186 was necessary, not only for high resolution but also to achieve proper alignment of particle
187 projections. To assess an alternative approach, we used Nb6 to develop a megabody,
188 termed 'Mb6', a fusion of a nanobody and a scaffold protein of either 45 or 86 kDa that
189 can serve as a larger fiducial marker, based on the work of Uchański *et al.*[6]. In that work,
190 the Mb designs employed for $GABA_A$ and WbaP produced cryo-EM maps that could not
191 resolve well past the nanobody portion, presumably due to flexibility. We thus opted
192 instead for using the c7HopQA12 design, which incorporates a twisted linker between the
193 nanobody and the 45 kDa HopQ scaffold to increase their contact and, ideally, rigidity.
194 However, our MD simulations suggested that even this design was characterized by
195 substantial flexibility between the Nb and scaffold (Extended Data Fig. 5a). In agreement
196 with this result, our cryo-EM 2D class averages of the MOR-Mb6 complex showed that
197 only the Nb6-receptor portion is well resolved, with the scaffold averaging out (Extended

198 Data Fig. 4b). Nevertheless, leveraging the ordered Nb6 portion of Mb6 in our cryo-EM
199 data, we obtained a 2.8 Å cryo-EM map (Fig. 3a, Extended Data Fig. 4) that provided an
200 unambiguous density for the ligand and receptor (Fig. 3c, Extended Data Fig. 8b). This
201 level of detail is quite comparable to the 2.8 Å crystal structure of MOR (Fig. 3b, d),
202 although the cryoEM map further resolves several probable water molecules in the ligand
203 binding site, including one that bridges interactions between the carboxylate of alvimopan
204 and the receptor (Extended Data Fig. 5b).

205 Comparing the binding poses of the MOR-selective alvimopan with that of the
206 structurally similar ligand JDTic, which is selective for KOR, reveals a striking difference.
207 Despite their similar scaffolds, the phenol-piperidine moieties of alvimopan and JDTic are
208 in completely different positions and orientations, nearly flipped in the binding pocket.
209 Aligning our structure with KOR-JDTic (PDB:4DJH[21]) reveals that JDTic would clash with
210 Y326$^{7.43}$ and Q124$^{2.60}$ in MOR, while alvimopan would clash with W124 and I294$^{6.55}$ in
211 KOR (I294$^{6.55}$ of KOR is substituted by a repositioned valine in MOR). In addition to the
212 steric confines of the binding pocket, charge differences also appear to contribute to the
213 differences in binding pose between JDTIC and alvimopan. The nitrogen of the
214 tetrahydroisoquinoline ring system of JDTic is likely also protonated or perhaps
215 protonated instead of the piperidine, and thus forms salt bridge interactions with D138$^{3.32}$
216 (D147$^{3.32}$ in MOR), just as the protonated piperidine of alvimopan does in MOR. Of note,
217 alvimopan shares similarities to fentanyl and its analogues, including a central piperidine
218 ring. Computational docking of carfentanil[22], a potent MOR agonist, in the active-state
219 structure of the receptor[3] suggests a pose similar to alvimopan, but with the additional
220 phenylamine moiety on the piperidine ring positioned to bind into the pocket occupied by

221 the toggle switch tryptophan W293$^{6.48}$ (Extended Data Fig. 5a). How a MOR ligand

222 engages this region is often the main determining factor for its agonism versus

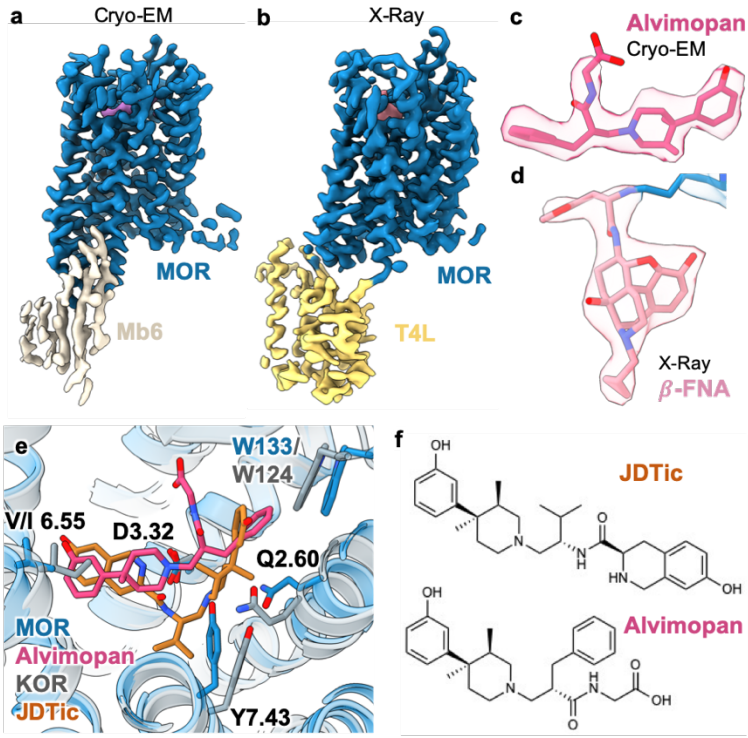

Fig 3. | Comparison of cryo-EM structure of alvimopan-bound MOR with crystal structures of MOR/β-FNA and KOR/JDTic
a, Cryo-EM map of MOR at 2.8 Å global resolution. **b,** 2Fo-Fc crystallography map of MOR at 2.8 Å contoured at σ=2.0. **c,** Cryo-EM density and model for inverse agonist alvimopan. **d,** Local 2Fo-Fc map around β-FNA contoured at σ=1.5. **e,** overlay of the alvimopan pose in the MOR cryo-EM structure (protein in blue, alvimopan in magenta) with the JDTic pose in the KOR crystal structure (protein in grey, JDTic in orange). **f,** Comparison of JDTic and alvimopan chemical structures highlighting similar phenol-piperidine scaffold.

223 antagonism, and we hypothesize that this phenyl moiety of fentanyl and its derivatives is

224 responsible for conversion of the piperidine scaffold to an agonist.

225

226

227 **Structure of SSTR2**

228 To test the cryo-EM/Nb6 approach on a receptor without prior structural

229 characterization we chose SSTR2, a member of the SSTR subfamily for which no

230 structures have been determined. Despite the absence of a stabilizing inverse agonist or

231 any other ligand and the lack of an energy filter in the microscope used for cryo-EM data

232 acquisition (typically beneficial for data quality when imaging small proteins), we were

233 able to obtain a 3.1 Å map of SSTR2/Nb6 with well-resolved features (Fig. 4a, Extended

234 Data Fig. 6, Extended Data Fig. 8c). Together with two active-state structures of SSTR2
235 bound to two different agonists, the endogenous 14-mer SST14 and the synthetic 8-mer
236 octreotide (detailed in our accompanying manuscript[23]), the inactive-state SSTR2
237 structure enabled us to characterize several aspects of receptor activation and ligand
238 recognition. Perhaps the most interesting feature of SSTR2 is the conformational flexibility
239 of ECL2; while in a well-defined position in the apo state structure, ECL2 is pushed to a
240 more open conformation when bound to the endogenous agonist SST14, but folds down
241 over the top of the receptor in the octreotide-bound state (Fig. 4b). As a consequence of
242 the ECL2 plasticity, different residues are engaged in binding the pan-SSTR agonist
243 SST14 versus the SSTR2-selective octreotide. This is an important factor to SSTR
244 subtype selectivity, which is explored further in the accompanying study[23].

245 Very few structures have been obtained to date for family A GPCRs in the
246 unliganded, apo state, primarily due to the general need for a stabilizing ligand to obtain
247 a crystal structure. Experimentally-derived apo structures provide an opportunity to
248 evaluate predicted structures from the recently published deep-learning based tools,
249 AlphaFold2[24] and RoseTTAfold[25]. Notably, while both software performed well in
250 predicting the overall structure of SSTR2, key details of the ligand binding site were in
251 disagreement with the experimental structure, particularly in residues D122$^{3.32}$, F92$^{2.53}$,
252 and Y302$^{7.43}$ (Fig. 4c), which are involved in ligand binding and activation, as detailed in
253 the companion active-state SSTR2 manuscript[23]. Although a more systematic
254 comparison is needed, this observation underscores both the merits but also the potential
255 limitations of homology model-based approaches. Differences in side chain positioning,

256 especially within a ligand binding site, can throw off structure-based drug discovery efforts

257 and other pursuits in which high-accuracy coordinates are required.

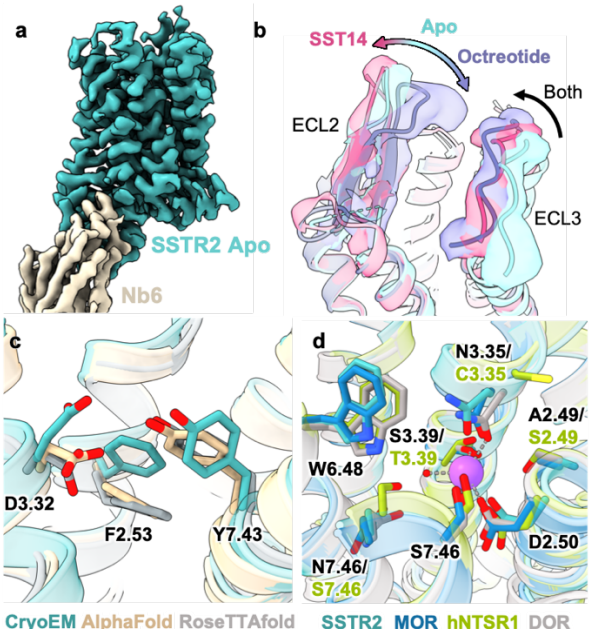

Fig 4. | Cryo-EM structure of the apo SSTR2 and comparison of sodium ion binding site.
a, Cryo-EM map of SSTR2 at 3.1 Å global resolution. **b,** Comparison of the model and cryo-EM maps of apo SSTR2 (teal) and SSTR2 in complex with either SST14 (magenta) or octreotide (purple). **d,** Overlay of SSTR2 (teal), MOR (blue), and NTSR1 (green) cryo-EM structures around the canonical family A sodium ion binding site with the DOR sodium coordination site structure (gray, PDB:4N6H).

258

259

260 **Differential sodium accommodation by family A GPCRs**

261 Our near-native inactive-state cryo-EM maps provide the opportunity to examine

262 the allosteric sodium binding site found deep in the core of many family A receptors. All

263 three of the receptors studied in this work have experimentally demonstrated negative

264 allosteric modulation by sodium[26–28]. In both MOR and SSTR2 the identities of the

265 residues in the sodium binding site are the same as the δ-opioid receptor (DOR), for which

266 there is a high-resolution crystal structure (1.8 Å) with a well-defined sodium site for

267 comparison[29] (Fig. 4c). The geometries of the MOR, SSTR2, and DOR sites are very

268 similar, with the exception of a slight rearrangement of $W^{6.48}$ in the case of both MOR

269 ($W293^{6.48}$) and SSTR2 ($W269^{6.48}$), and $N125^{3.35}$ in SSTR2. In contrast to SSTR2 and

270 MOR, hNTSR1 has four amino acid differences in the sodium binding site, namely

271 T155$^{3.39}$ (in place of S$^{3.39}$), S357$^{7.46}$ (in place of N$^{7.46}$), S111$^{2.49}$ (in place of A$^{2.49}$), and
272 C151$^{3.35}$ (in place of N$^{3.35}$). In the DOR structure, both S135$^{3.39}$ and N131$^{3.35}$ directly
273 interact with the sodium .

274 The three maps we determined resolve features consistent with water and/or ions
275 in the canonical sodium binding region near D2.50, although only NTSR1 has sufficiently
276 high resolution in this particular region to facilitate unambiguous ion modeling (Extended
277 Data Fig. 7a-c). The probable ion sites of SSTR2 and MOR match relatively well to those
278 observed in DOR. In the hNTSR1 map, we observe a density with close proximity to
279 oxygen atoms of T155$^{3.39}$, S111$^{2.49}$, D112$^{2.50}$ (Extended Data Fig. 7a). Even though
280 precise identification of water versus ion is challenging in cryo-EM maps, we expect that
281 this feature corresponds to the sodium, shifted by 1.8 Å compared to the sodium in DOR
282 (Fig. 4d, Extended Data Fig. 7d, e). As other receptors with resolved sodium ion sites
283 have cysteine or other hydrophobic residues in place of N$^{3.35}$, S111$^{2.49}$ is likely responsible
284 for the shift in sodium position in NTSR1. Overall, we find substantial similarity between
285 the sodium binding sites of inactive state GPCRs from cryo-EM and crystallography.

286

287 **Discussion**

288 Here, we present inactive-state structures of three family A GPCRs, all obtained
289 by cryo-EM at resolutions as high as 2.4 Å by employing minimal engineering and a
290 universal nanobody for projection alignment. By using molecular dynamics simulations to
291 assess fiducial markers for use in cryo-EM structure determination, we could accurately
292 predict that Nb6 is sufficiently rigid for cryo-EM particle alignment, while Mb6 is too flexible
293 for resolution beyond the nanobody portion. Each of the obtained cryo-EM structures

294 yields new insights into ligand recognition, with resolution that is as good or better than
295 that of analogous structures produced by x-ray crystallography. In contrast to active state
296 GPCR-G protein complexes, where the highest-resolution portion of the map is on the
297 larger G protein due to the center of alignment, the inactive-state Nb6 GPCR structures
298 display their highest resolution at the receptor core, facilitating accurate modeling of
299 ligands and their surrounding hydration. This generalizable approach opens this broad
300 family of drug targets to rapid, crystallization-free structure determination, with
301 biochemical stability of the receptor and nanobody binding being the only limitations. As
302 such, we anticipate Nb6 to be a broadly applicable approach to determining inactive state
303 structures of near-native GPCRs, further propelling drug discovery in this class of
304 receptors.
305
306 **Author Contributions**
307 M.J.R. cloned constructs, expressed and purified proteins, processed EM data, built
308 models, and ran/analyzed molecular dynamics simulations. F.H. cloned constructs and
309 expressed proteins. J.M. performed BRET assays. A.S. prepared cryo-EM samples and
310 collected cryo-EM data. M.C. expressed proteins and purified nanobody. O.P. prepared
311 cryo-EM samples and collected cryo-EM data. T.C. provided constructs for nanobody
312 expression and BRET assays. M.J.R. and G.S. wrote the manuscript with input from F.H.,
313 J.M., O.P., and T.C.. G.S. supervised the project.
314
315 **Data Availability**

316 All data generated or analyzed in this study are included in this article and the
317 Supplementary Information. The cryo-EM density maps and corresponding coordinates
318 have been deposited in the Electron Microscopy Data Bank (EMDB) and the Protein Data
319 Bank (PDB), respectively, under the following accession codes: Raw data has been
320 deposited in EMPIAR under the following accession codes:
321
322 **Competing Interests**
323 The authors declare no competing interests.
324
325 **Acknowledgements**

326 We thank the Kobilka lab for providing plasmids of NTSR1 and MOR. Cryo-EM data
327 were collected at the Stanford cryo-EM center (cEMc) with support from E. Montabana.
328 This work was supported, in part, by the Mathers Foundation (G.S.), training grant
329 T32GM089626 (J.G.M.), and used the Extreme Science and Engineering Discovery
330 Environment (XSEDE)[30] resource comet-gpu through sdsc-comet allocation TG-
331 MCB190153 (G.S.), which is supported by National Science Foundation grant number
332 ACI-1548562.

333
334 **Methods**
335
336 **Cloning**

337 The cDNA for SSTR2 was obtained from Horizon Discovery and cloned into a pFastBac
338 vector containing an N-terminal haemagglutinin (HA) signal sequence followed by a FLAG
339 epitope (DYKDDDD) and a C-terminal C3 protease cleavage site followed by enhanced
340 green fluorescent protein (eGFP) and a hexahistidine (His6) tag using Gibson cloning.
341 Constructs for hNTSR1 and MOR were obtained from the lab of Brian Kobilka and have
342 been described previously[3,19]. Briefly, each is cloned in pFastBac with an N-terminal
343 haemagglutinin (HA) signal sequence followed by a Flag epitope (DYKDDDD) and a C-
344 terminal HRV 3C protease cleavage site followed by a hexahistidine (His6) tag. In the
345 case of hNTSR1, the His6 tag is preceded by enhanced green fluorescent protein (eGFP).
346 For MOR, two point mutations (M264L and K269R) were introduced with site-directed
347 mutagenesis; PCR reactions were conducted with Q5 polymerase with the following pair
348 of primers: 5'- GGCTCCCGCGAAAAGGACAGGAACCTGCGC -3'; 5'-
349 CGACAGCAGGCGGACACTCTTGAG
350 -3'. For hNTSR1, residues between T247$^{5.59}$ to L277$^{6.3}$ of kappa opioid were substituted
351 with site-directed mutagenesis in three steps, with the following three primer pairs: 5'-
352 ATCACACGCCTGGTTCTGGCAGTGGTCATCGCCT
353 -3' 5'- AATATCATCAGGGTGTACAGGACCGAGATGACCA -3'; 5'-
354 GGAATCTGCGCCGAATCACACGCCTGGTTCT -3' 5'-
355 ACAGATTTCAGCCGCAATATCATCAGGGTGTACAG-3'; 5'-
356 GCCGCTCAGCAGGCGCACAGATTTCAGCCGCA -3' 5'-
357 AGCCGCGAAAAGGATCGGAATCTGCGCCGAAT -3'. For SSTR2, residues between
358 S238 and K252 were replaced with those of kappa opioid in two steps with site-directed

359 mutagenesis with the following primer pair: 5'-
360 GAGCGGCAGCTCTAAGAGGAAGAAGTCTGAGAA
361 -3' 5'- AGCAGGCGCACGGACTTCACCTTGATGATAATGAAC
362 -3'; 5'- CGGAATCTGCGCAAGGTCACCCGAATGGTG
363 -3', 5'- ATCCTTTTCGCGGCTGCCGCTCAGCA
364 -3'.

365 **Biolumescence resonance energy transfer (BRET) assays**

366 BRET assays were performed and analyzed as previously described[4] with the following
367 modifications: HEK-293S cells grown in FreeStyle 293 suspension media (Thermo
368 Fisher) were transfected at a density of 1 million cells/mL in 2 mL volume using 600 ng
369 total DNA at 1:1 ratio of Receptor-rLuc:Nb6-mVenus and a DNA:PEI ratio of 1:5,
370 and incubated in a 24 deep well plate at 220 rpm, 37°C for 48 hours. Cells were harvested
371 by centrifugation, washed with Hank's Balanced Salt Solution (HBSS) without
372 Calcium/Magnesium (Gibco), and resuspended in assay buffer (HBSS with 20 mM
373 HEPES pH 7.45) with 1 µg/mL freshly prepared coelenterazine h (Promega). Cells were
374 plated in white-walled, white-bottom 96 well plates (Costar) in a volume of 60 µl/well and
375 60,000 cells/well. Ligands were prepared in drug buffer (assay buffer with 0.1% BSA, 6
376 mM $CaCl_2$, 6 mM $MgCl_2$), and added at a 1:2 ratio of drug:cell suspension. Ten minutes
377 after the addition of ligand, plates were read using a SpectraMax iD5 plate reader using
378 485 nm and 535 nm emission filters with a one-second integration time per well. The
379 computed BRET ratios (mVenus/RLuc emission) were normalized to ligand-free control
380 (Net BRET) prior to further analysis.
381

382 **Expression and Purification of Nb6 and Mb6**

383 Wk6 *E. coli* (ATCC) were transformed via heat shock with Nb6 plasmid[4] and two 5 mL
384 starter cultures were grown overnight in LB supplemented with 100 μg/ml ampicillin. 2L
385 of terrific broth were supplemented with 100 μg/ml ampicillin, inoculated with starter
386 cultures, and grown at 37°C with shaking until OD_{600}=0.7. Expression was then induced
387 with 1mM IPTG and expression was allowed to proceed at 28°C overnight. Pellets were
388 harvested via centrifugation and washed once with phosphate-buffered saline before
389 snap freezing in liquid nitrogen. Pellets containing Nb6 were thawed and resuspended in
390 50 mM Tris pH 8.0, 0.5 mM EDTA, 20% w/v sucrose (TES) buffer at 15 mL / 1 liter pellet
391 and supplemented with protease inhibitor cocktail and shaken in an orbital shaker for 1
392 hour at 4°C. An additional 30 mL per 1 liter pellet of TES diluted 1:4 with water was added
393 and placed in an orbital shaker for an additional 45 minutes at 4°C. Cell debris was
394 removed by ultracentrifugation at 100,000xg for 30 minutes. The supernatant was filtered
395 with a 45 micron filter, supplemented with 20 mM imidazole, and loaded over a gravity Ni-
396 NTA column at 4°C. The column was washed with 10 CV of a buffer containing 250 mM
397 NaCl, 50 mM Tris pH 7.5, 10 mM imidazole, and then eluted with buffer containing 250
398 mM imidazole. Nanobody was concentrated and applied to size exclusion
399 chromatography with a buffer containing 250 mM NaCl and 50 mM Tris pH 7.5.
400 Monomeric fractions were pooled, concentrated, supplemented with 10% glycerol, and
401 snap frozen in liquid nitrogen for later use. Expression and purification of Mb6 was
402 performed identically to Nb6.

403

404 **Expression and Purification of Receptor/Nb6 Complexes**

405 All receptors were expressed in Sf9 insect cells (Expression Systems) infected at a
406 density of 3-4 million cells/ml. At 48 hours post-infection, cells were collected with
407 centrifugation, washed with phosphate-buffered saline containing 10 μM antagonist
408 (when used), and pellets were snap frozen in liquid nitrogen for purification. A general
409 protocol was used for producing receptor/Nb6 complexes (Extended Data Fig. 1), with
410 some slight deviations. Sf9 pellets containing receptor were lysed in hypotonic buffer
411 containing 20 mM HEPES pH 7.5, 5 mM $MgCl_2$, protease inhibitor cocktail, benzonase,
412 10 μM antagonist (when used), and 2 mg/ml iodoacetamide and gently stirred for an hour
413 at 4°C. Membranes were harvested with ultracentrifugation at 100,000xg, supernatant
414 was discarded, and membranes were resuspended in solubilization buffer containing 250
415 mM NaCl, 20 mM HEPES pH 7.5, 1 mM $MgCl_2$, protease inhibitor cocktail, 10 μM
416 antagonist (when used), and 2 mg/ml iodoacetamide; then drip frozen into liquid nitrogen
417 and stored at -80°C. Resuspended membranes were thawed and detergent was added
418 dropwise while stirring at 4°C to a final concentration of 1% LMNG/0.1% CHS/0.1%
419 Cholate. After 3 hours, insoluble debris was removed with ultracentrifugation at 100,000
420 g. Solubilized receptor was supplemented with 20 mM imidazole and gravity loaded over
421 a Ni-NTA resin column. Columns were washed with 10 column volumes of buffer
422 containing 250 mM NaCl, 20 mM HEPES pH 7.5, 10 μM antagonist (when used), 20 mM
423 imidazole, and 0.1% LMNG/0.01% CHS and protein was eluted in buffer containing 250
424 mM NaCl, 20 mM HEPES pH 7.5, 10 μM antagonist (when used), 250 mM imidazole, and
425 0.01% LMNG/0.001% CHS. Receptor was then supplemented with 5 mM $CaCl_2$ and
426 loaded onto M1 flag resin; washed with 5 column volumes of 250 mM NaCl, 20 mM
427 HEPES pH 7.5, 10 μM antagonist (when used), 2 mM CaCl2, and 0.1% LMNG/0.01%

428 CHS; and eluted with buffer containing 150 mM NaCl, 20 mM HEPES pH 7.5, 10 μM
429 antagonist (when used), 1 mM EDTA, 0.2 mg/ml FLAG peptide, and 0.1% LMNG/0.01%
430 CHS. Purified receptor was incubated on ice overnight with HRV 3C protease and purified
431 Nb6 was added at a 2:1 molar ratio. Receptor/Nb6 complex was concentrated in a 50
432 kDa molecular weight cutoff spin concentrator and subjected to SEC chromatography
433 with an ENrich 650 column (Bio-Rad) and a buffer containing 150 mM NaCl, 20 mM
434 HEPES pH 7.5, 0.001% LMNG, 0.00033% GDN, and 0.0001% CHS. Fractions containing
435 monomeric receptor/Nb6 complex were pooled for cryo-EM sample preparation. This
436 protocol was identical for SSTR2 and NTSR1 with the exception of the addition of 100
437 μM TCEP to the lysis buffer for NTSR1. Preparation of MOR/Mb6 complex was identical
438 to that of receptor Nb6 complex, with the omission of the HRV-3C cleavage to remove
439 eGFP as it was not present in the construct.
440
441 **Cryo-EM Sample Preparation**
442 All samples were prepared on glow-discharged holey gold grids (Quantifoil ultrAufoil
443 R1.2/1.3), blotted in a FEI Vitrobot Mark IV (Thermo Fisher Scientific) at 4°C and 100%
444 humidity, and plunge frozen into liquid ethane. Blotting conditions for each sample were
445 as follows: 3.0 μl of NTSR1/Nb6 complex at 16 mg/ml with an additional 0.05% beta OG;
446 3.0 μl of MOR/Mb6 complex at 5 mg/ml; and 2.5 μl of SSTR2/Nb6 complex at 16 mg/ml
447 with an additional 0.05% beta OG.
448
449 **Cryo-EM Data Collection**

450 All samples were collected on a KRIOS electron microscope at an accelerating voltage
451 of 300 kV, with an energy filter for NTSR1/Nb6 and MOR/Mb6 and without an energy filter
452 for SSTR2/Nb6. All data was collected through SerialEM with beam tilt compensation and
453 recorded on a Gatan K3 direct electron detector. The resulting image stacks have a pixel
454 size of 0.434 Å for NTSR1/Nb6 and MOR/Mb6 and 0.426 Å for SSTR2/Nb6, all in super
455 resolution mode. Each NTSR1/Nb6 image stack is composed of 71 frames with an
456 incident electron dose of 0.85 $e^-/Å^2$ per frame, for a total dose of 61 $e^-/Å^2/s$ per micrograph.
457 Each MOR/Mb6 image stack is composed of 63 frames with an incident electron dose of
458 0.98 $e^-/Å^2$ per frame, for a total dose of 61 $e^-/Å^2/s$ per micrograph. Each SSTR2/Nb6
459 image stack is composed of 55 frames with an incident electron dose of 1.26 $e^-/Å^2$ per
460 frame, for a total dose of 69 $e^-/Å^2/s$ per micrograph.
461
462 **Cryo-EM Data Processing**
463 A pictorial depiction of each cryoEM processing workflow can be found in Extended Data
464 Figs. 2c, 4c, and 6c. Briefly, dose-fractionated image stacks were imported into RELION-
465 3.1[31] and subjected to beam-induced motion correction and dose weighting with
466 MotionCor2[32]. Contrast transfer function parameter estimation was performed with
467 CTFFIND-4.1[33]. Particle selection and extraction was performed with the Laplacian
468 autopicker function of RELION-3.1 on micrographs with a CTF fit better than 3.5 Å. The
469 extracted particle stack was imported into CryoSPARC[34] and subjected to multiple rounds
470 of 2D classification followed by iterative rounds of *ab initio* reconstruction with multiple
471 classes and heterogeneous refinement to further classify particles. In early 3D iterations,
472 particles from poor 3D classes were subjected to additional 2D classification and good

473 particles were 'rescued' for further 3D classification. Once iterative *ab initio* and
474 heterogenous refinement no longer produced higher resolution reconstruction, particles
475 were re-imported to RELION-3.1. In the cases of hNTSR1 and MOR CTF fit cutoffs of 3.1
476 Å and 3.3 Å were applied, respectively. Particles were then subjected to 3D refinement in
477 RELION-3.1 followed by Bayesian polishing. Polished particles were then imported back
478 to CryoSPARC for non-uniform refinement, global CTF refinement based on optics group,
479 and repeated non-uniform and local refinement.
480
481 **Model Building and Refinement**
482 All initial models were rigid body fit into cryo-EM maps using the ChimeraX[35] software.
483 For hNTSR1, the cryo-EM model of active state hNTSR1 was used as the initial model
484 (PDB:6OS9[19]); for MOR the crystal structure of inactive MOR bound to a covalent
485 antagonist was used as the initial model (PDB:4DKL[36]), and for SSTR2 a homology model
486 generated from KOR (PDB:6VI4[4]) was used. In all cases KOR/Nb6 complex (PDB:6VI4[4])
487 was aligned to the receptor to produce the initial model for the nanobody. All structures
488 were manually refined in COOT[37] with iterative real-space refinement in Phenix[38]. Once
489 accurate modeling was achieved for the protein components, the GemSpot pipeline[39] was
490 used for automatic modeling of the ligands alvimopan and SR48692 into MOR and
491 hNTSR1 respectively. Final refinement was executed in Phenix, followed by model-free
492 Phenix map modification for NTSR1 and MOR[40]. All maps displayed in this work are those
493 prior to model-free map modification unless stated otherwise.
494
495 **Molecular Dynamics Simulations**

496 Simulations of the KOR/Nb6 complex started with the crystal structure PDB:6VI4, with the
497 pose of JDTic replaced with that of PDB:4DJH[21]. Maestro's protein preparation tool was
498 used to assign protonation states, optimize hydrogen bonding, and build missing
499 sidechains and loops. Once the receptor was prepared, the orientation of proteins in
500 membranes webserver (OPM)[41] was used to align the receptor as it would be in a
501 membrane in the xy plane and the CHARMM-GUI[42] was used to build the full system with
502 a 1-palmitoyl-2-oleoyl-*sn*-glycero-3-phosphocholine POPC/CHS lipid bilayer, TIP3P
503 water[43], and 150 mM NaCl. PSF and PDB files were generated with the OPLS-AA/M[44]
504 forcefield in VMD[45] for the system. For Mb6, a homology model was built from PDB:6XVI
505 with the Prime homology modeling tool[46]. This model was solvated in TIP3P water and
506 150 mM NaCl in VMD for simulation.

507 Molecular dynamics simulations were carried out in NAMD[47] with a 2 fs timestep
508 with SHAKE and SETTLE algorithms[48,49], with a Langevin thermostat and a Nosé-Hoover
509 Langevin piston barostat at 1 atm with a period of 50 fs and decay of 25 fs. Periodic
510 boundary conditions were used with nonbonded interactions smoothed starting at 10 Å to
511 12 Å with long-range interactions treated with particle mesh Ewald (PME). The system
512 was minimized for 1,500 steps and then slowly heated from 0 to 303.15K in increments
513 of 20K simulating for 0.4 ns at each increment. For the Kappa/Nb6 simulations, all non-
514 hydrogen, non-water, and non-ion atoms were restrained with a 1 kcal/mol/ $Å^2$ harmonic
515 restraint during heating and an additional 10 ns of equilibration. 1 kcal/mol/ $Å^2$ harmonic
516 restraints were used for an additional 10 ns of equilibration on all non-hydrogen protein
517 atoms followed by a final 10 ns of restrained equilibration with 1 kcal/mol/ $Å^2$ harmonic
518 restraint on only $C\alpha$ atoms. The first 30 ns of unrestrained molecular dynamics were also

519 considered to be equilibration, with an additional 500 ns of simulation performed. All
520 simulations were performed in triplicate. For Mb6, the first 30 ns of unrestrained molecular
521 dynamics were treated as equilibration, and 100 ns of triplicate molecular dynamics
522 simulations were performed.

523 **Docking**

524 The cryo-EM structure of active MOR (PDB:6DDE)[3] was prepared in Maestro and
525 carfentanil was docked with Glide XP docking[50].

526

527 **References**

528 1. Robertson, M. J., Meyerowitz, J. G. & Skiniotis, G. Drug discovery in the era of cryo-
529 electron microscopy. *Trends in Biochemical Sciences* (2021).
530 doi:10.1016/j.tibs.2021.06.008

531 2. Hauser, A. S., Attwood, M. M., Rask-Andersen, M., Schiöth, H. B. & Gloriam, D. E. Trends
532 in GPCR drug discovery: New agents, targets and indications. *Nat. Rev. Drug Discov.*
533 (2017). doi:10.1038/nrd.2017.178

534 3. Koehl, A. *et al.* Structure of the μ-opioid receptor-Gi protein complex. *Nature* **558**, 547–552
535 (2018).

536 4. Che, T. *et al.* Nanobody-enabled monitoring of kappa opioid receptor states. *Nat. Commun.*
537 (2020). doi:10.1038/s41467-020-14889-7

538 5. Gully, D. *et al.* Biochemical and pharmacological profile of a potent and selective
539 nonpeptide antagonist of the neurotensin receptor. *Proc. Natl. Acad. Sci. U. S. A.* (1993).
540 doi:10.1073/pnas.90.1.65

541 6. Uchański, T. *et al.* Megabodies expand the nanobody toolkit for protein structure
542 determination by single-particle cryo-EM. *Nat. Methods* (2021). doi:10.1038/s41592-020-
543 01001-6

544 7. Zimmerman, D. M. *et al.* Discovery of a Potent, Peripherally Selective trans-3,4-Dimethyl-
545 4-(3-hydroxyphenyl)piperidine Opioid Antagonist for the Treatment of Gastrointestinal
546 Motility Disorders. *J. Med. Chem.* (1994). doi:10.1021/jm00041a003
547 8. Carraway, R. & Leeman, S. E. Characterization of radioimmunoassayable neurotensin in
548 the rat. Its differential distribution in the central nervous system, small intestine, and
549 stomach. *J. Biol. Chem.* (1976). doi:10.1016/s0021-9258(17)32938-1
550 9. Christou, N. *et al.* Neurotensin pathway in digestive cancers and clinical applications: an
551 overview. *Cell Death and Disease* (2020). doi:10.1038/s41419-020-03245-8
552 10. Liu, J. *et al.* neurotensin receptor 1 antagonist SR48692 improves response to carboplatin
553 by enhancing apoptosis and inhibiting drug efflux in ovarian cancer. *Clin. Cancer Res.*
554 (2017). doi:10.1158/1078-0432.CCR-17-0861
555 11. Volkow, N. D. & Blanco, C. The changing opioid crisis: development, challenges and
556 opportunities. *Molecular Psychiatry* (2021). doi:10.1038/s41380-020-0661-4
557 12. Volkow, N. D. & Collins, F. S. The Role of Science in Addressing the Opioid Crisis. *N. Engl.*
558 *J. Med.* (2017). doi:10.1056/nejmsr1706626
559 13. Günther, T. *et al.* International union of basic and clinical pharmacology. CV. somatostatin
560 receptors: Structure, function, ligands, and new nomenclature. *Pharmacol. Rev.* (2018).
561 doi:10.1124/pr.117.015388
562 14. Ballesteros, J. A. & Weinstein, H. Integrated methods for the construction of three-
563 dimensional models and computational probing of structure-function relations in G protein-
564 coupled receptors. *Methods Neurosci.* (1995). doi:10.1016/S1043-9471(05)80049-7
565 15. Stoeber, M. *et al.* A Genetically Encoded Biosensor Reveals Location Bias of Opioid Drug
566 Action. *Neuron* (2018). doi:10.1016/j.neuron.2018.04.021
567 16. Deluigi, M. *et al.* Complexes of the neurotensin receptor 1 with small-molecule ligands
568 reveal structural determinants of full, partial, and inverse agonism. *Sci. Adv.* (2021).
569 doi:10.1126/sciadv.abe5504

570 17. Mittl, P. R., Ernst, P. & Plückthun, A. Chaperone-assisted structure elucidation with
571 DARPins. *Current Opinion in Structural Biology* (2020). doi:10.1016/j.sbi.2019.12.009
572 18. Scott, D. J., Kummer, L., Egloff, P., Bathgate, R. A. D. & Plückthun, A. Improving the apo-
573 state detergent stability of NTS1 with CHESS for pharmacological and structural studies.
574 *Biochim. Biophys. Acta - Biomembr.* (2014). doi:10.1016/j.bbamem.2014.07.015
575 19. Kato, H. E. *et al.* Conformational transitions of a neurotensin receptor 1–Gi1 complex.
576 *Nature* **572**, 80–85 (2019).
577 20. Russo, C. J. & Passmore, L. A. Ultrastable gold substrates for electron cryomicroscopy.
578 *Science (80-.).* (2014). doi:10.1126/science.1259530
579 21. Wu, H. *et al.* Structure of the human κ-opioid receptor in complex with JDTic. *Nature* (2012).
580 doi:10.1038/nature10939
581 22. Van Bever, W. F. M., Niemegeers, C. J. E. & Schellekens, K. H. L. P. A. J. N 4 substituted
582 1 (2 arylethyl) 4 piperidinyl N phenylpropanamides, a novel series of extremely potent
583 analgesics with unusually high safety margin. *Arzneimittel-Forschung/Drug Res.* (1976).
584 23. Robertson, M. J., Meyerowitz, J. M., Panova, O., Borrelli, K. W., Skiniotis, G. Plasticity in
585 Ligand Recognition at Somatostatin Receptors. (2021)
586 24. Tunyasuvunakool, K. *et al.* Highly accurate protein structure prediction for the human
587 proteome. *Nature* (2021). doi:10.1038/s41586-021-03828-1
588 25. Baek, M. *et al.* Accurate prediction of protein structures and interactions using a three-track
589 neural network. *Science (80-.).* (2021). doi:10.1126/science.abj8754
590 26. Kong, H., Raynor, K., Yasuda, K., Bell, G. I. & Reisine, T. Mutation of an aspartate at
591 residue 89 in somatostatin receptor subtype 2 prevents Na+ regulation of agonist binding
592 but does not alter receptor-G protein association. *Mol. Pharmacol.* (1993).
593 27. Martin, S., Botto, J. M., Vincent, J. P. & Mazella, J. Pivotal role of an aspartate residue in
594 sodium sensitivity and coupling to G proteins of neurotensin receptors. *Mol. Pharmacol.*
595 (1999). doi:10.1124/mol.55.2.210

596 28. Yabaluri, N. & Medzihradsky, F. Regulation of μ-opioid receptor in neural cells by
597 extracellular sodium. *J. Neurochem.* (1997). doi:10.1046/j.1471-4159.1997.68031053.x
598 29. Fenalti, G. DRUG DISCOVERY Molecular control of delta -opioid receptor signalling. *Nat.*
599 *-LONDON-* (2014).
600 30. Towns, J. *et al.* XSEDE: Accelerating scientific discovery. *Comput. Sci. Eng.* (2014).
601 doi:10.1109/MCSE.2014.80
602 31. Zivanov, J. *et al.* RELION-3: New tools for automated high-resolution cryo-EM structure
603 determination. *bioRxiv* (2018). doi:10.1101/421123
604 32. Zheng, S. Q. *et al.* MotionCor2: Anisotropic correction of beam-induced motion for
605 improved cryo-electron microscopy. *Nature Methods* **14**, 331–332 (2017).
606 33. Rohou, A. & Grigorieff, N. CTFFIND4: Fast and accurate defocus estimation from electron
607 micrographs. *J. Struct. Biol.* **192**, 216–221 (2015).
608 34. Punjani, A., Rubinstein, J. L., Fleet, D. J. & Brubaker, M. A. CryoSPARC: Algorithms for
609 rapid unsupervised cryo-EM structure determination. *Nat. Methods* (2017).
610 doi:10.1038/nmeth.4169
611 35. Pettersen, E. F. *et al.* UCSF ChimeraX: Structure visualization for researchers, educators,
612 and developers. *Protein Sci.* (2021). doi:10.1002/pro.3943
613 36. Manglik, A. *et al.* Crystal structure of the μ-opioid receptor bound to a morphinan
614 antagonist. *Nature* (2012). doi:10.1038/nature10954
615 37. Emsley, P., Lohkamp, B., Scott, W. G. & Cowtan, K. Features and development of Coot.
616 *Acta Crystallogr. Sect. D Biol. Crystallogr.* **66**, 486–501 (2010).
617 38. Adams, P. D. *et al.* PHENIX: A comprehensive Python-based system for macromolecular
618 structure solution. *Acta Crystallogr. Sect. D Biol. Crystallogr.* **66**, 213–221 (2010).
619 39. Robertson, M. J., van Zundert, G. C. P., Borrelli, K. & Skiniotis, G. GemSpot: A Pipeline for
620 Robust Modeling of Ligands into Cryo-EM Maps. *Structure* (2020).
621 doi:10.1016/j.str.2020.04.018

622 40. Terwilliger, T. C., Ludtke, S. J., Read, R. J., Adams, P. D. & Afonine, P. V. Improvement of
623 cryo-EM maps by density modification. *Nat. Methods* (2020). doi:10.1038/s41592-020-
624 0914-9
625 41. Lomize, M. A., Pogozheva, I. D., Joo, H., Mosberg, H. I. & Lomize, A. L. OPM database
626 and PPM web server: Resources for positioning of proteins in membranes. *Nucleic Acids*
627 *Res.* **40**, (2012).
628 42. Lee, J. *et al.* CHARMM-GUI Input Generator for NAMD, GROMACS, AMBER, OpenMM,
629 and CHARMM/OpenMM Simulations Using the CHARMM36 Additive Force Field. *J.*
630 *Chem. Theory Comput.* **12**, 405–413 (2016).
631 43. Jorgensen, W. L., Chandrasekhar, J., Madura, J. D., Impey, R. W. & Klein, M. L.
632 Comparison of simple potential functions for simulating liquid water. *J. Chem. Phys.* **79**,
633 926–935 (1983).
634 44. Robertson, M. J., Tirado-Rives, J. & Jorgensen, W. L. Improved Peptide and Protein
635 Torsional Energetics with the OPLS-AA Force Field. *J. Chem. Theory Comput.* **11**, 3499–
636 3509 (2015).
637 45. Humphrey, W., Dalke, A. & Schulten, K. VMD: Visual molecular dynamics. *J. Mol. Graph.*
638 **14**, 33–38 (1996).
639 46. Jacobson, M. P. *et al.* A Hierarchical Approach to All-Atom Protein Loop Prediction.
640 *Proteins Struct. Funct. Genet.* (2004). doi:10.1002/prot.10613
641 47. Phillips, J. C. *et al.* Scalable molecular dynamics with NAMD. *Journal of Computational*
642 *Chemistry* **26**, 1781–1802 (2005).
643 48. Ryckaert, J. P., Ciccotti, G. & Berendsen, H. J. C. Numerical integration of the cartesian
644 equations of motion of a system with constraints: molecular dynamics of n-alkanes. *J.*
645 *Comput. Phys.* (1977). doi:10.1016/0021-9991(77)90098-5
646 49. Miyamoto, S. & Kollman, P. A. Settle: An analytical version of the SHAKE and RATTLE
647 algorithm for rigid water models. *J. Comput. Chem.* (1992). doi:10.1002/jcc.540130805

648 50. Friesner, R. A. *et al.* Extra precision glide: Docking and scoring incorporating a model of
649 hydrophobic enclosure for protein-ligand complexes. *J. Med. Chem.* **49**, 6177–6196
650 (2006).
651